Structural deformations and mechanical properties of Si$_2$BN under uniaxial and uniform biaxial strain in comparison with graphene: An *ab initio* study

Zacharias G. Fthenakis[1,2] and Madhu Menon[3]

[1]*Department of Physics, University of South Florida, Tampa, Florida 33620, USA*
[2]*Institute of Electronic Structure and Laser, FORTH, P.O. Box 1527, 71110 Heraklio, Crete, Greece*
[3]*Department of Physics and Astronomy, University of Kentucky, Lexington, Kentucky 40506, USA*

Si$_2$BN has been recently predicted theoretically as a new entirely planar two-dimensional material with a honeycomblike structure (like graphene), which is stable even at $T > 1000$ K. In the present paper, we study the structural deformations and mechanical properties of Si$_2$BN and graphene under both uniaxial (along the direction of the arm chair and zigzag chains) and uniform biaxial tensile strain till the fracture limit and we compare those properties of the two structures with each other. According to our findings, in the Si$_2$BN structure, Si–Si and Si–B bonds are weaker than B–N and Si–N bonds, respectively, contrary to graphene bonds, which all have the same strength. In particular, B–N bond lengths of Si$_2$BN remain almost unchanged under the strain conditions we studied, not exceeding $\approx 6\%$ of their initial length. Si$_2$BN was found to be anisotropic, exhibiting large Young's and biaxial modulus values of the order of 1/3 and 2/5 of that of graphene, respectively. The different bond strengths in Si$_2$BN explains its anisotropy and makes it behave very differently under strain when compared to graphene.

I. INTRODUCTION

The last decade has seen a tremendous surge of interest in two-dimensional (2D) materials due to their unique properties, which can be significantly different from those of their three-dimensional (3D) counterparts [1]. Many such materials have been theoretically predicted (see, for instance, Refs. [2–17]), however, only a few of them have been observed or synthesized experimentally [18–21]. Among the 2D materials there exists a very interesting sub-category of structures that are one atom thick and also entirely flat. Graphene [18] and boron nitride [16,22] (BN) are representative structures for this category that have been observed experimentally [19]. However, both have notable disadvantages for nanoelectronics applications; graphene has no gap while BN has a very large gap.

On the other hand, silicene [3], which is the Si counterpart of graphene, was found to be a buckled structure—a feature also shared by most of the 2D Si containing honeycomblike structures [7–11]. Furthermore, very few among these structures were found to be planar[11,12].

Recently, the existence of a stable new 2D material (Si$_2$BN) has been theoretically predicted [23]. It constitutes parallelly arranged Si dimers in a hexagonal lattice which are interconnected through B–N dimers as shown in Fig. 1. It can be seen as an extensively doped silicene structure, which has the advantage that it is entirely flat without any dangling bonds and extremely stable kinetically [23], contrary to the original silicene, which (as stated) is buckled and kinetically unstable, with dangling bonds which make it highly reactive [3]. The Si$_2$BN planarity gives rise to the unusual sp^2-like hybridization for the Si atoms. Interestingly, the p_z orbitals on Si, normal to the structure plane, interact with the neighboring Si $- p_z$ orbitals, thus leading to the creation of Si–Si double

bonds. This has the effect of eliminating the dangling bonds which would otherwise make it energetically and kinetically unstable. The Si$_2$BN can, therefore, considered to be the latest addition to a very rare class of Si-based 2D honeycomblike structures that are entirely planar.

Recent studies suggest that the proposed Si$_2$BN monolayer is efficient for hydrogen storage [24] and has a wider absorption range than graphene, thus making Si$_2$BN a promising candidate for euryphotic photosensitive detector applications [25]. Furthermore, it is proposed to be a high capacity anode material for Li and Na ion batteries [26], surpassing the capacity of many other 2D materials including graphene and phosphorene. Moreover, its structure has inspired the design and study of other similar materials like the family of Pb$_2$XY 2D topological insulators, with X = Ga/In and Y = Sb/Bi [27], the family of Ge$_x$(BN)$_y$ structures [28] and the IV-V-VI compounds [29]. Other similar Si$_2$BN structures have also been studied recently [30]. These studies show the Si$_2$BN to be a very interesting material with potential for useful nanotechnology applications.

So far, the mechanical properties of Si$_2$BN have not been studied. In the present paper, we cover this gap by studying the response of Si$_2$BN to uniaxial and uniform biaxial strain up to the fracture limit and we compare them with graphene. For our study on the response of Si$_2$BN to uniaxial strain, we focus on two high-symmetry strain directions: (i) along the Si–Si bonds (indicated as e_{ac}) and (ii) along the perpendicular direction (indicated as e_{zz}), which correspond to the arm chair and zigzag directions of graphene, respectively, and are shown in Fig. 1. For graphene, we similarly focus on the arm chair and zigzag chain directions, also indicated as e_{ac} and e_{zz}, respectively. The results obtained for the mechanical behavior of Si$_2$BN under strain for these high-symmetry directions can
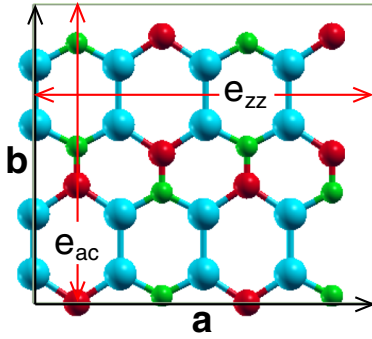
FIG. 1. Figure showing the 32-atom rectangular unit cell of the Si_2BN structure used in the present paper along with the strain directions, e_{zz} and e_{ac}. Vectors **a** and **b** are the unit cell vectors. Light blue, red, and green spheres represent Si, B, and N atoms, respectively.

also be used to obtain results for other strain directions using the method described in Ref. [31], which reported the study of mechanical behavior of graphene under strain for any arbitrary strain directions. For the study of Si_2BN under uniform biaxial strain conditions, equal strain is applied simultaneously in both e_{ac} and e_{zz} directions.

For all these cases, we plot the stress-strain and the energy-strain curves, which we use to calculate the Young's and the biaxial moduli, as well as the Poisson's ratio, the speed of sound and the ultimate tensile strain (UTS), the corresponding stress values, and the fracture limits. Contrary to graphene, the presence of different atom species results in different bond strengths in Si_2BN. Specifically, Si–Si and Si–B bonds were found to be weaker than B–N and Si–N bonds, respectively. B–N bond lengths remain almost unchanged under the strain conditions we studied, not exceeding ≈6% of their initial length, even under the extreme strain conditions. These result in the anisotropic mechanical properties for the Si_2BN, while also exhibiting high Young's and biaxial moduli, which are of the order of 1/3 and 2/5 of those of graphene, respectively, as well as high UTS values, thus providing further support to the high stability of the material found using other methods in an earlier work [23].

II. THE METHOD

For the calculations of the present paper, we use the density-functional theory (DFT) method as implemented in the SIESTA code [32]. For the exchange and correlation functional, we utilize the generalized gradient approximation (GGA) and the Perdue-Burke-Ernzerhof (PBE) functional [33]. For the pseudopotentials of Si, B, N, and C, which are used in our calculations, we utilize the norm-conserving Troullier-Martins pseudopotentials [34] in the Kleinman-Bylander factorized form [35], which can be found in the GGA pseudopotential database of SIESTA [36]. The basis for the wave-function expansion in real space is an atomiclike double-zeta basis with polarization orbitals for each atom. Calculations are performed in reciprocal space, using a $10 \times 10 \times 1$ Monkhorst-Pack [37] k-point grid for both Si_2BN and graphene. The mesh cutoff energy for the determination of

charge densities and potentials used in the calculations for Si_2BN and graphene is 500 and 300 Ry, respectively. For these mesh cutoff values and k-grid points, the total energy per atom converges to a certain value with an error which is less than 0.1 meV.

For the calculations of both Si_2BN and graphene, we adopt a 32-atom unit cell in a rectangular lattice, with lattice vectors **a** $= (a, 0)$ and **b** $= (0, b)$, as shown in Fig. 1. 20 Å of vacuum, separating layers of Si_2BN, is used in the calculations to simulate an isolated Si_2BN layer. The same vacuum space is also used for graphene. Optimizations are performed for fixed lattice vectors using the conjugate gradient method. The unstrained structure is assumed to be fully optimized if the maximum atomic force and the maximum stress component become smaller than 0.001 eV/Å and 0.01 GPa, respectively. The same criteria apply for the optimized structure under uni-axial strain, excluding the strain component along the strain direction, which obviously takes a nonzero value, while for uniform biaxial strain only the criterion for the forces apply, since the strained structure under uniform biaxial strain has fixed lattice vectors. For the stress calculation along the plane of the Si_2BN and graphene sheets, we assume a structural thickness of 3.34 Å as in graphite. This consideration is also used in the above optimization criterion for maximum stress since it allows direct comparisons of the mechanical properties of 2D structures with graphite [2]. For the derivation of the optimized structure (i.e., for strain $\varepsilon = 0$), the lattice vectors are varied since the above optimization criteria are achieved. For the study of Si_2BN under uniaxial strain along the e_{zz} and e_{ac} directions, the length of the unit-cell vector in the strain direction (i.e., the length a for strain along e_{zz} and b for strain along e_{ac}) is kept fixed at a specific value, corresponding to a chosen strain value, while the length of the unit-cell vector perpendicular to it is allowed to vary till the optimization criteria for the strained structures are reached, as stated above. For the study of Si_2BN under uniform biaxial strain, the lengths of both unit-cell vectors **a** and **b** are strained simultaneously under the same strain value.

Optimizations under strain ε are performed for increasing strain values starting from 0 up to the fracture limit with an increment of 0.01. The initial atomic positions of a structure under optimization for strain $\varepsilon = \varepsilon_0$ have the same fractional coordinates with those of the optimized structure under strain $\varepsilon = \varepsilon_0 - 0.01$.

III. RESULTS AND DISCUSSION

A. Equilibrium Si_2BN and graphene structure at $\varepsilon = 0$

According to our findings, the fully optimized 32-atom unit cell of Si_2BN (shown in Fig. 1) consists of a rectangle with the unit-cell vectors **a** and **b** with lengths a = 12.841 Å and b = 11.293 Å, respectively. For the analogous 32-atom graphene unit cell, which is also a rectangle, the corresponding unit-cell vectors were found to be $a = 4\sqrt{3}a_0 = 9.9572$ Å and $b = 6a_0 = 8.6232$ Å, where $a_0 = 1.4372$ Å is the bond length of graphene. Interestingly, for these a and b values the area mass density, ρ_S, of graphene and Si_2BN are almost equal to each other, taking the values $\rho_S = 0.743$ mgr/m^2 for graphene and $\rho_S = 0.742$ mgr/m^2 for Si_2BN.
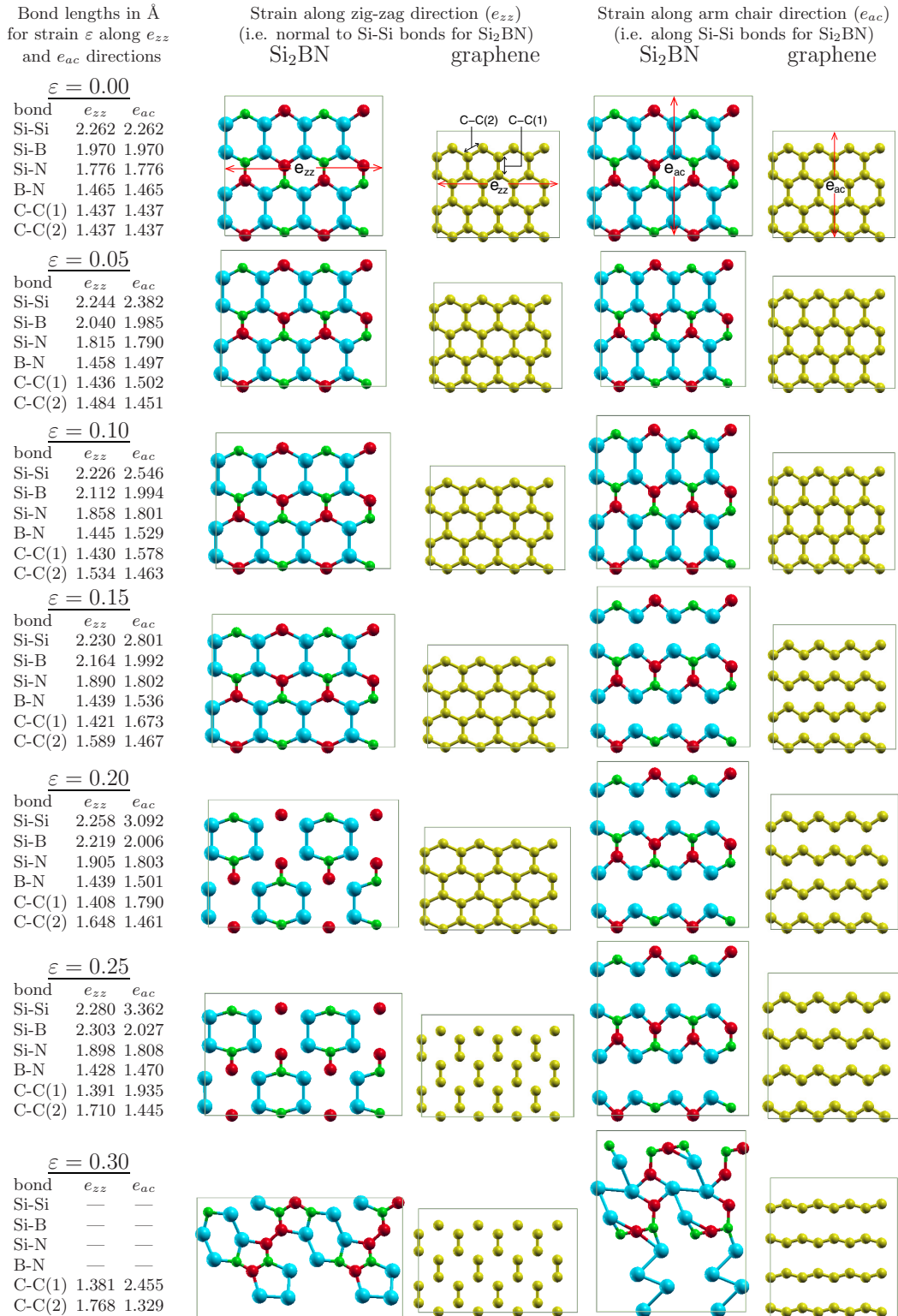
FIG. 2. Structural deformations of Si_2BN and graphene for tensile strain along e_{zz} and e_{ac} directions. Same colors are used for atoms as in Fig. 1. The strain values ε, as well as the length of the bonds for each case, are shown in the first column. Strain is increased from 0.00 to 0.30 in 0.05 steps.

B. Structure deformations and bond-length changes under uniaxial strain

The structural deformations obtained from stretching Si_2BN and graphene uniaxially along e_{zz} and e_{ac} directions are shown in Fig. 2 for increasing strain values in 0.05 strain steps. The figures for Si_2BN and graphene are placed side by side for ease of comparison. The first column of the figure lists the nearest-neighbor bond lengths for both structures. As
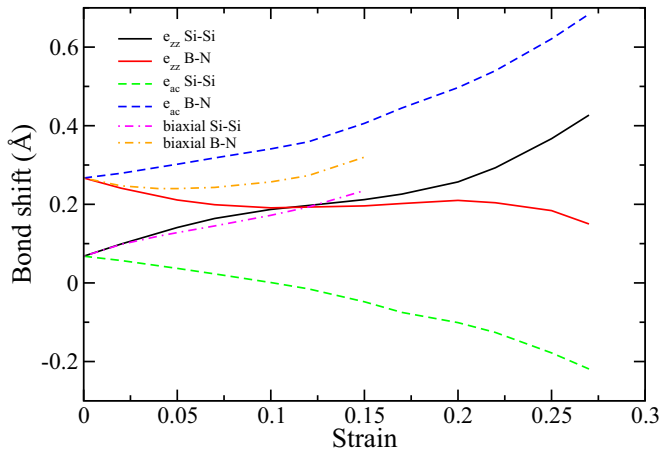
FIG. 3. Shift of Si–Si and B–N bonds for uniaxial strain along e_{zz} and e_{ac} direction, as well as, uniform biaxial strain. (See text for details.)

seen in this column, the C–C(1) bonds of graphene correspond to the bonds along the e_{ac} direction, while the C–C(2) bonds correspond to the bonds of the zigzag chains along the e_{zz} direction. For the illustration purposes of Fig. 2, we consider that a C–C, Si–Si, and Si-B bond breaking occurs if its length exceeds the equilibrium length by 15%, 20.5%, and 12%, respectively, or 1.65 Å, 2.73 Å, and 2.21 Å, respectively. The justification for this choice of values will be provided later.

A general feature of both graphene and Si$_2$BN, under uniaxial strain for the two strain directions e_{zz} and e_{ac}, is that bonds which are oriented along the e_{ac} direction (i.e., Si–Si and B–N bonds for Si$_2$BN and C–C(1) bonds for graphene) remain parallel to each other, preserving the initial bond direction for $\varepsilon = 0$. In particular, B–N bonds of Si$_2$BN are located along parallel straight lines oriented along the e_{ac} direction, while alternating B–N and N–B bonds, which are normal to the same straight line, are shifted with each other along e_{ac} direction. The opposite happens for the Si–Si bonds, however. Si atoms of the Si–Si bonds which are normal to the same straight line are located along parallel straight lines and, consequently, no shift of the Si–Si bonds along the e_{ac} direction is seen, as happens with B–N bonds. However, Si–Si bonds along a line in the e_{ac} direction exhibit an alternating shift with each other with respect to the normal to that line (i.e., along e_{zz} direction). These shifts can be clearly seen in Fig. 2 and they are caused by the difference in the length of the Si–N and Si–B bonds (as well as the different Si–NSi and Si-B-Si angles), which break the symmetry of the perfect honeycomb lattice.

In Fig. 3, we plot these shifts as a function of strain, where we can see that for $\varepsilon = 0$ those shifts are both positive. As strain increases, the shifts of Si-Si bonds for strain along the e_{zz} direction also increase, while the shifts of B–N bonds decrease. For strain along the e_{ac} direction, however, the shifts of B–N bonds increase as a function of strain, while the shifts of Si-Si bonds decrease. The shifts of Si-Si bonds become zero at $\varepsilon \approx 0.10$ and become negative upon a further increase in the strain value. These negative values correspond to an increase in the shift of their absolute value, with the alternatingly shifted Si-Si bonds crossing the imaginary line between them

along the e_{ac} direction. Thus, an increase in strain along the e_{zz} direction results in a larger Si–Si bond length in the hexagon containing two B atoms than the Si–Si bond length in the hexagon containing two N atoms. For increasing strain along the e_{ac} direction, the former is larger than the latter up to a strain value $\varepsilon \approx 0.10$ at which they become equal to each other and for $\varepsilon \gtrsim 0.10$ the former becomes smaller than the latter. It is also worth noting that the shift in B–N bonds for strain along the e_{zz} direction reaches a local minimum for $\varepsilon \approx 0.10$ and a local maximum for $\varepsilon \approx 0.20$, although the difference between those maximum and minimum values is approximately 0.02 Å, indicating that the shift in B–N bonds remains practically constant for a large strain range between approximately 0.06 and 0.25. As for graphene, due to the high symmetry of the structure, there is no reason for such shifts of bonds to occur.

As seen in Fig. 2, as the strain along the e_{ac} direction is increased, the C–C(1) bonds eventually break and graphene dissociates into disconnected zigzag chains. For $\varepsilon \gtrsim 0.3$, these zigzag chains tend to deform into linear carbon chains, as shown in the last row of Fig. 2. Similarly, when the strain along the e_{zz} direction is increased, C–C(2) bonds eventually break and graphene dissociates into disconnected C–C dimers, as shown in the same row of Fig. 2. It is worth noting, however, that the formation of graphene strips or ribbons is also possible from the breaking of C–C graphene bonds, which is not described in Fig. 2. These results agree with other theoretical results presented in the literature for graphene [2].

Unlike graphene, however, the Si$_2$BN structure contains four different types of bonds with different bond strengths. Consequently, the dissociation here follows a different sequence as shown in Fig. 2. As the tensile strain along the e_{ac} direction is increased, the Si–Si bonds are the first to break ($\varepsilon \gtrsim 0.15$). Similarly, as the strain along the e_{zz} direction is increased, the Si–B bonds can be seen to break first ($\varepsilon \gtrsim 0.20$). Bearing in mind that (i) the Si–Si and B–N bonds are oriented along the e_{ac} strain direction and (ii) the Si–N and Si–B bonds have almost the same tilting angle with the e_{zz} strain direction, we conclude that the Si–Si bonds are weaker than the B–N bonds. Similarly, it can be surmised that the Si–B bonds are weaker than the Si–N bonds.

The breaking of the Si–Si bonds under the strain along the e_{ac} direction leads to the dissociation of the Si$_2$BN structure into disconnected narrow Si$_2$BN strips, while the Si–B bond breaking under the strain along the e_{zz} direction causes the dissociation of the Si$_2$BN structure into (Si$_2$BN)$_2$ flakes, as both are shown in Fig. 2. As the strain is increased further ($\varepsilon > 0.27$) in both e_{zz} and e_{ac} directions, the Si$_2$BN structure further deforms into two rather irregular structures, losing its planarity. The deformed irregular structures found for $\varepsilon = 0.3$ are shown in the last row of Fig. 2. Overall, as our strain studies suggest, the Si$_2$BN structure is extremely robust, even at high strain values, and almost comparable to graphene.

In Figs. 4(a) and 4(b), we plot the relative bond-length differences [defined as $(d - d_0)/d_0$, where d_0 is the equilibrium bond length (corresponding to $\varepsilon = 0$) and d is the bond length for $\varepsilon \neq 0$] for the bonds of Si$_2$BN and graphene, respectively, as a function of strain. As can be seen in Fig. 4(a), for strain $0 \leqslant \varepsilon \lesssim 0.12$ along the e_{ac} direction, there is a monotonic increase in both the Si–Si and B–N
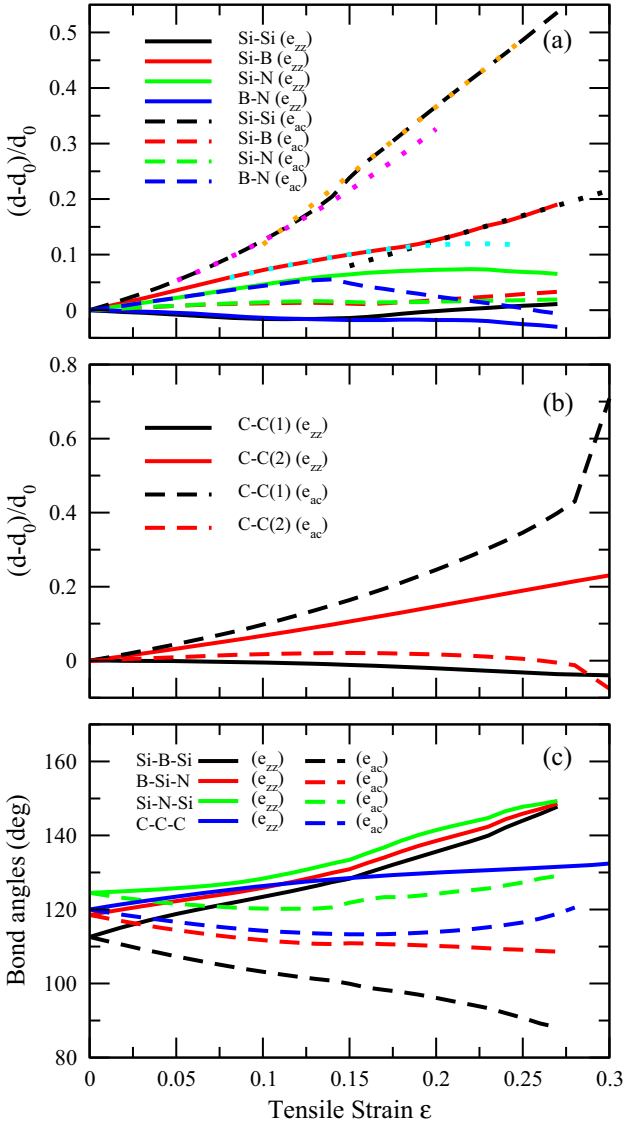
FIG. 4. Bond and angle deformations under tensile strain along e_{zz} (solid lines) and e_{ac} (dashed lines) directions. (a), (b) Relative bond-length differences $(d - d_0)/d$, (where d and d_0 are the bond lengths at $\varepsilon \neq 0$ and $\varepsilon = 0$, respectively), for the bonds of Si$_2$BN and graphene, respectively. (c) Angle deformations for the Si–B–Si, B–Si–N, and Si–N–Si angles of Si$_2$BN, and C–C–C angles of graphene formed along zigzag chains in the e_{zz} direction. Dotted lines in (a) are presented as a guide to the eye, to indicate different slopes.

bond lengths, which are parallelly oriented along the strain direction. In the range $0.12 \lesssim \varepsilon \lesssim 0.15$, however, the slope of the Si–Si relative bond-length difference changes as shown by the corresponding dotted lines of Fig. 4(a), while the B–N relative bond-length difference reaches its maximum at $\varepsilon = 0.14$ and is then followed by a decrease. This behavior can be explained as follows: For applied strain $\varepsilon < 0.14$, both Si–Si and B–N bond lengths increase with an increase in the strain value. At $\varepsilon = 0.14$, the Si–Si bond starts breaking and the Si$_2$BN structure dissociates into Si$_2$BN zigzag strips. As ε is increased further: (i) the already weak Si–Si interactions become even weaker, causing the dissociation of the Si$_2$BN structure into weakly interacting disconnected Si$_2$BN strips

and (ii) the interactions between the dissociated Si$_2$BN strips become even weaker, causing the shrinkage of the initially stretched B–N bonds. It is reasonable, therefore, to conclude that the Si–Si bonds start breaking when the slope of the Si–Si curve of Fig. 4(a) changes, or the maximum of the B–N curve is reached; i.e., for $\varepsilon = 0.14$. For this strain value, the Si–Si bond length is 2.73 Å, or 20.5% larger than its value at equilibrium. This explains the reason for assigning this value for the Si–Si bond breaking limit. For strain along the e_{ac} direction in the range $0 \leqslant \varepsilon \leqslant 0.3$, the maximum increase in the B–N bond length is only 5.6%, while for the Si–N and Si–B bonds it is even less—only 3%, having almost the same behavior as a function of ε. Therefore, a bond breaking of B–N, Si–N, and Si–B bonds cannot be achieved.

The graphene counterparts of both Si–Si and B–N bonds of Si$_2$BN are the C–C(1) bonds of graphene, while the counterparts of both Si–B and Si–N bonds are the C–C(2) bonds. As shown in Fig. 4(b), for applied stress along the e_{ac} direction, there is an increase in the C–C(1) bonds as a function of strain, eventually leading to the dissociation of the structure into zigzag strips. The C–C(2) bonds, on the other hand, remain mostly unchanged, increasing slightly in the range $0 \leqslant \varepsilon \leqslant 0.15$ and then decreasing for $\varepsilon > 0.15$, attaining maximum value (2.1% increase) at $\varepsilon = 0.15$. Using this observation, and using similar reasoning as used in the case for Si$_2$BN, it is reasonable to assume that the C–C(1) bond breaking starts when the C–C(2) bond length start decreasing, i.e., at $\varepsilon = 0.15$, for which the C–C(1) bond length is 1.65 Å, or 15% longer than its length at equilibrium.

As shown in Fig. 4(a), as the strain value is increased along the e_{zz} direction, the increase in the Si–B bond length is more than that for the Si–N bond, and consequently the Si–B bonds can be expected to break first. For strain in the range $0.18 \lesssim \varepsilon \lesssim 0.20$, the slope of the Si–B curve of Fig. 4(a) increases, indicating a weakening of the Si–B bonds, while the Si–N bond lengths continue to increase up to $\varepsilon = 0.22$ and are then followed by a decrease. Based on this observation, one may assume that the Si–B bond breaking starts for strain in the range $0.18 \lesssim \varepsilon \lesssim 0.22$, for which the Si–B bond length takes values between 2.19–2.25 Å, or 11.4–14.3% longer than the Si–B bond length at equilibrium. The maximum Si–N bond length, which is obtained at $\varepsilon = 0.22$, is 1.91 Å, corresponding to an increase of the equilibrium bond-length value by 7.38%. The Si–Si and B–N bonds, which for strain along the e_{zz} direction are oriented normal to the strain direction, remain practically unchanged with a maximum change in the absolute value of 3% for strain in the range $0 \leqslant \varepsilon \leqslant 0.3$. As a result, only the Si–B bonds are stretched enough to break, thus forming the (Si$_2$BN)$_2$ flakes shown in Fig. 2. Interestingly, if all the Si–B bonds do not break simultaneously (i.e., due to the lattice vibrations, which could compress some Si–B bonds and stretch others), then a variety of arm-chair-type ribbons or irregular shape arm-chair-type flakes may be produced, which are expected to have B and Si atoms at the edges.

In stark contrast to the differing responses of the Si–B and Si–N bonds of the Si$_2$BN structure under applied strain, their graphene counterparts [the C–C(2) bonds] have the same response under strain. This is expected since all bonds connect the same species of atoms. Under these conditions, if all such bonds break simultaneously, this will lead to the disconnected
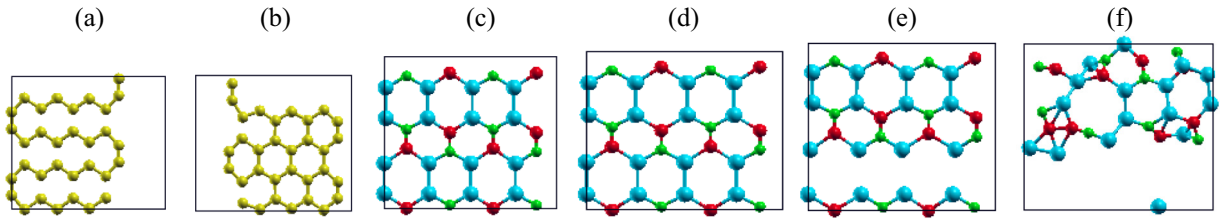
FIG. 5. Structural deformations of Si_2BN and graphene under uniform biaxial strain. Same colors are used for atoms as in Fig. 1. (a) Graphene for $\varepsilon = 0.18$, (b) graphene for $\varepsilon = 0.21$, (c) Si_2BN for $\varepsilon = 0.05$, (d) Si_2BN for $\varepsilon = 0.10$, (e) Si_2BN for $\varepsilon = 0.13$, and (f) Si_2BN for $\varepsilon = 0.15$.

C–C dimers shown in Fig. 2. If, on the other hand, they do not break simultaneously [i.e., due to lattice vibrations, which could stretch or compress the C–C(2) bonds], it will lead to the dissociation of the graphene structure into arm-chair-type ribbons or irregularly shaped nanoflakes.

In Fig. 4(c), we show the deformation as a function of strain for the Si–B–Si, B–Si–N, and Si–N–Si angles of the Si_2BN, and C–C–C angles of graphene, which are formed along the zigzag chains in the e_{zz} direction. Due to symmetry reasons, the sum of Si–B–Si and Si–N–Si angles equals twice that of the B–Si–N angle and, therefore, the B–Si–N angle can be considered as an average of the Si–B–Si and Si–N–Si angles. The values of those angles at $\varepsilon = 0$ are $(Si - B - Si) = 112.58^o$, $(B - Si - N) = 118.53^o$ and $(Si - N - Si) = 124.49^o$, while $(C - C - C) = 120^o$. As expected, for strain along the e_{zz} direction those angles increase, while for strain along the e_{ac} direction, they decrease. This trend should continue at least up to a certain strain value, while beyond that they may have a different behavior depending on the structural deformations that take place and, in particular, may lead to bond weakening or breaking. As shown in Fig. 4(c), this trend is followed by Si–B–Si and B–Si–N angles up to the fracture limit, but Si–N-Si angle of Si_2BN and the C–C–C angle of graphene for strain along the e_{ac} direction follow it only up to their minimum value, which for Si–N–Si is 120.16° at $\varepsilon = 0.11$ and for C–C–C is 113.30° at $\varepsilon = 0.16$. This behavior is due to the competition between the Si_2BN and graphene structures at $\varepsilon = 0$, with their corresponding dissociated structures resulting from the breaking of the Si–Si and C–C(1) bonds, respectively, when the strain value along e_{ac} direction exceeds the critical value for the breaking of those bonds. Thus, for increasing strain along the e_{ac} direction, those angles will initially decrease and then, depending on the competition between those two structures, they may either continue to decrease or they may increase until reaching the angles of their corresponding dissociated strip structures. In our case, they both increase, while Si–B–Si and B–Si–N further decrease. This competition is affected by the weakening (as strain increases) of the Si–Si and C–C(1) bonds of Si_2BN and graphene, respectively. Note that, for strain along the e_{ac} direction, both of these bonds undergo the maximum possible elongation of a bond of the structure for a certain strain value, since they are oriented along the strain direction.

C. Structure deformations and bond-length changes under uniform biaxial strain

As expected (due to the isotropy of graphene) graphene bonds increase linearly with the increasing strain up to the

fracture limit and they all have the same length for a specific strain value. This is clearly shown in Fig. 6, where the relative bond-length differences $(d - d_0)/d_0$ of the Si_2BN and graphene bonds under uniform biaxial strain conditions are presented. Under these conditions, all graphene bonds would break simultaneously if strain exceeded a critical value, fracturing the structure to single atoms. This possibility, however, is rather unlikely given that the symmetry breaking resulting from lattice vibrations can allow some bonds to break before reaching the critical value. Another possibility is a phase transformation (possibly assisted by the lattice vibrations) that would lower the symmetry and the energy of the structure, thus leading to a more stable structure. In the case of graphene, we find that for strain $\varepsilon > 0.17$, the strained graphene structure becomes unstable and a phase transformation takes place, transforming the unstable high-symmetric strained graphene structure to a less symmetric but stable snakelike chain shown in Fig. 5(a). Further increase in the strain leads to the formation of other structures that include graphene flakes, which may or may not be connected with each other with a few bonds, as shown in Fig. 5(b).

On the other hand, due to its anisotropy, Si_2BN will behave differently under uniform biaxial strain conditions. Figures 5(c)–5(f) show some snapshots of the structural deformations of Si_2BN under uniform biaxial strain for increasing strain values, in accordance with Fig. 2. According to our findings, for strain $\varepsilon \geqslant 0.13$ the strained Si_2BN becomes unstable (see details in the Supplemental Material (SM) [38]),
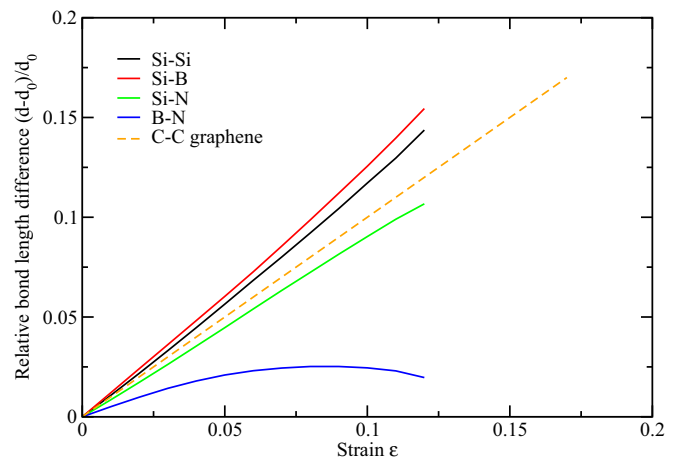

FIG. 6. Relative bond-length differences $[(d - d_0)/d_0]$ for Si_2BN and graphene bonds under uniform biaxial strain versus strain.

leading to the structure shown in Fig. 5(e), where one can see that the Si–Si bonds at the bottom of the figure have been broken. It is worth noting that although the relative elongation of Si–B bonds is slightly larger than that of the Si–Si bonds (as shown in Fig. 6), the Si–Si bonds breaking occurs first as strain increases, leading to the formation of the ribbons, which are shown in Fig. 5(e). However, any further increase in strain results in the breaking of the Si–B bonds, which is followed by a rearrangement of the atoms and, finally, the structure transforms to a nonplanar amorphous cluster as shown in Fig. 5(f).

As in the case of graphene, the strain value for fracturing Si$_2$BN under uniform biaxial strain is smaller than the corresponding values for uniaxial strain, which is reasonable when one considers that the biaxial strain combines simultaneously the action of both ε_{zz} and ε_{ac}, which in this case act synergistically for the fracture of the structure.

Moreover, as one can see in Fig. 6, B–N bonds do not increase by more than $\approx 2.5\%$ (a value which is achieved at $\varepsilon = 8.5\%$), indicating that those bonds will not break under uniform biaxial strain conditions, in accordance with the results found for uniaxial strain along the e_{ac} direction. Furthermore, the decrease in the B–N bonds elongation for increasing strain for $\varepsilon > 8.5\%$ points to a significant weakening of the Si–Si bonds for these values and could be considered as the starting point for bond breaking under these strain conditions.

As for the shifts of Si–Si and B–N bonds, which were discussed in the case of uniaxial strain, they also occur in the case of uniform biaxial strain. In Fig. 3, we show those shifts as a function of strain. As one can see, the corresponding shift for Si–Si bonds, which were discussed in the previous subsection, follows a curve very similar to that obtained for uniaxial strain along the e_{zz}, while the shift of B–N bonds follows a curve that looks like an average of the corresponding shifts for strain along the e_{ac} and e_{zz} directions, exhibiting a minimum at $\varepsilon \approx 0.05$.

D. Mechanical properties of Si$_2$BN under uniaxial strain. Comparison with graphene

In Figs. 7(a)–7(d), we present the strain energy per atom, ΔU, the stress, σ (stress-strain curve), the Poisson's ratio, ν, and the Young's modulus, E, as a function of strain ε along both the e_{zz} and e_{ac} directions for both Si$_2$BN and graphene in the strain range $-0.05 \leqslant \varepsilon \leqslant 0.3$. Energy and stress calculations have been performed for increasing strain values in this range, with a 0.01 strain step. By strain energy per atom ΔU, we mean the difference $\Delta U = U - U_0$, where U and U_0 are the values of the total energy per atom for the strained structure along a specific strain direction and at $\varepsilon = 0$, respectively.

Since Si$_2$BN as well as graphene are 2D structures, it is more appropriate to define stress as force per unit length instead of force per unit area as in 3D materials. However, we may add a width of 3.34 Å to each of the planar
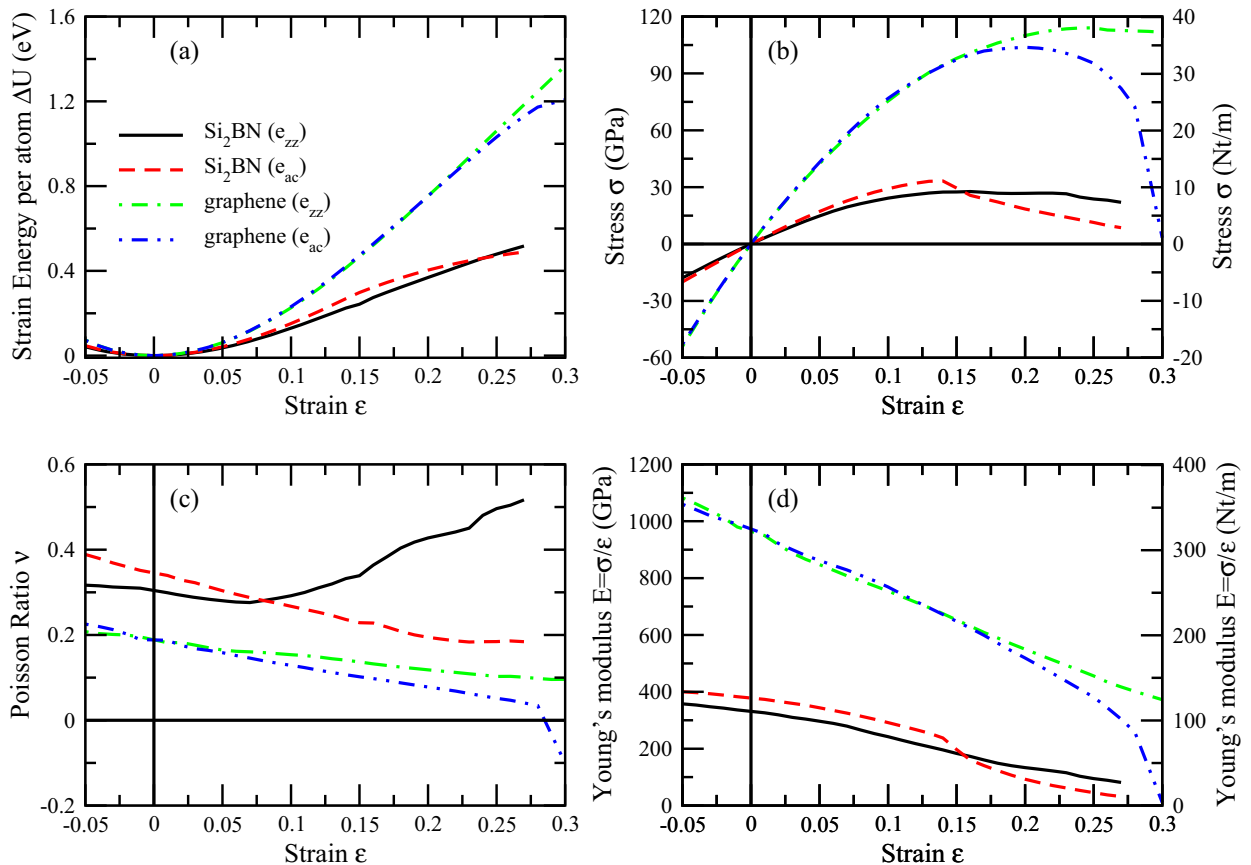

FIG. 7. Mechanical response of Si$_2$BN under uniaxial strain along e_{zz} and e_{ac} directions and comparison with graphene. (a) Strain energy per atom $\Delta U = (U - U_0)/N$, (b) stress-strain plot, (c) Poisson's ratio ν, and (d) Young's modulus $E = \sigma/\varepsilon$.

TABLE I. Mechanical properties (Young's modulus, E, Poisson's ratio, ν, area density, ρ_s, speed of sound, v_s, ultimate tensile stress, σ_u, and the corresponding strain ε_u) of Si_2BN in comparison with graphene, silicene, and boronitrene for tensile strain along the strain directions e_{zz} and e_{ac}. Q.E. stands for QUANTUM ESPRESSO. CA stands for Ceperley and Adler functional. Values in parenthesis are either not provided by the corresponding paper and have been evaluated by us, or they have been re-evaluated by us assuming the 3.34 Å width whenever necessary.

Structure	Study	Direction	E (GPa)	E (Nt/m)	ν	ρ_S (mgr/m^2)	v_s (km/sec)	ε_u	σ_u (GPa)	σ_u (Nt/m)
Si_2BN	Present paper	e_{zz}	330	110	0.303	0.742	12.2	0.16	27.68	9.245
Si_2BN	Present paper	e_{ac}	376	125	0.345	0.742	13.0	0.14	33.26	11.11
Graphene	Present paper	e_{zz}	964	322	0.190	0.743	20.8	0.25	114.0	38.08
Graphene	Present paper	e_{ac}	964	322	0.189	0.743	20.8	0.20	103.8	34.66
Graphene	LDA/CA—VASP [7]		(1003)	335	0.16					
Graphene	GGA/PBE—GAUSSIAN [16]		(1150)	345	0.149	0.749	(21.5)			
Graphene	GGA/PBE—SIESTA [39]	e_{zz}	(967)	323	0.179					
Graphene	GGA/PBE—Q.E. [2]	e_{ac}	1024	342	0.177	0.686	21.14	0.185	103	34.4
Graphene	GGA/PBE—Q.E. [2]	e_{zz}	1020	341	0.173	0.686	21.10	0.225	114	38.1
Graphene	Exp. [40]		1020 ± 150	341 ± 50				0.25	126 ± 12	42 ± 4
Silicene	LDA–DMol^3 [41,42]	e_{zz}	(188.6)	63.0	0.31			0.15		
Silicene	LDA–DMol^3 [41,42]	e_{ac}	(188.6)	63.0	0.31			0.17		
Silicene	LDA/CA–VASP [7]		(186)	62	0.30					
Silicene	GGA/PBE—SIESTA [43]	e_{zz}	(186.8)	(62.4)						
Silicene	GGA/PBE—SIESTA [43]	e_{ac}	(176.9)	(59.1)						
Silicene	GGA/PBE—VASP [44]	e_{zz}	(179.8)	60.06	0.41			0.14		5.66
Silicene	GGA/PBE—VASP [44]	e_{ac}	(190.1)	63.51	0.37			0.18		7.07
Boronitrene	LDA/CA—VASP [7]		(799)	267	0.21					
Boronitrene	GGA/PBE—GAUSSIAN [16]		(905)	271	0.211	0.736	(19.2)			

structures which would correspond to the interlayer separation of graphite to allow for direct comparisons [2] between the two 2D materials (Si_2BN and graphene) and graphite. In the present paper, we adopt both considerations in Figs. 7(b) and 7(d), where strain units are used. In the left y axis of these figures, normal stress units are used (adopting the 3.34 Å plane width), while in the right y axis the force per unit length units (Nt/m) is used. For the calculation of the Young's modulus, E, we use the relation $E = \sigma/\varepsilon$, for the Poisson's ratio, ν, the relation, $\nu = -\varepsilon_\perp/\varepsilon$, where $\varepsilon_\perp$ is the transverse contraction strain caused as a result of the normal strain ε and for the speed of sound, v_s, the relation $v_s = \sqrt{E/\rho_s}$, where E is the Young's modulus in force per length units and ρ_s the area density.

Although a negative strain (which corresponds to compression) would just cause structural bending, computationally it is possible to simulate the response of the nonbended planar structure to negative strain [2]. This allows for a more reliable estimation of the Young's modulus and Poisson's ratio [2] without the need for the extrapolation of the corresponding curves of Fig. 7 to zero strain.

Our calculated results for graphene are in relatively good agreement with the other *ab initio* methods, as well as results obtained using the same method and the SIESTA suite [39].

Using the least-squares-fitting method to fit the stress, σ, the Young's modulus, E, and the Poisson's ratio, ν, to quadratic and linear functions of strain, ε, we can have a good estimation of E and ν for strain along the e_{zz} and e_{ac} directions. Details of the fits are shown in the SM [38], while the values of Young's modulus, E, the Poisson's ratio, ν, the speed of sound, v_s, as well as the ultimate tensile stress, σ_U, and the corresponding strain, ε_U, are shown in Table I.

As can be seen from both Fig. 7 and Table I, in terms of E and ν, Si_2BN is anisotropic (in contrast to graphene), exhibiting rather large E values, which are as high as $\approx 0.34-0.39$ times the value of E for graphene. The Poisson's ratio values are higher than the corresponding ν value of graphene by 1.6–1.8. The speed of sound, v_s, which is calculated using the relation $v_s = \sqrt{E/\rho_S}$, is also high; it is larger than $1/2$ of the corresponding v_s of graphene. The ultimate tensile stress σ_u, although not as high as in graphene, is still high enough, corresponding approximately to $1/4$–$1/3$ of the σ_u value for graphene, appearing at a lower strain values (0.14–0.16 for Si_2BN; 0.20–0.25 for graphene).

When compared to silicene, however, the Si_2BN appears to be very robust [7,41–44]. Picturing Si_2BN as a highly doped silicene structure, we can say that the presence of B and N atoms have the effect of enhancing its mechanical properties since the Si–Si bond is less strong when compared to the Si–B, Si–N, and B–N bonds. Moreover, the rippling features of silicene have been completely eliminated and the Si_2BN structure is entirely planar.

An interesting point worth discussion is the very different behavior between the Poisson's ratio of Si_2BN as a function of strain, for strain along the e_{ac} and e_{zz} directions. For strain along e_{ac}, the Poisson's ratio appears to exhibit an almost linear behavior as a function of strain and the same behavior is also observed for graphene for both the e_{ac} and e_{zz} directions. On the other hand, for strain along the e_{zz} direction the Poisson's ratio shows an initial decrease followed by an increase. As explained in the SM [38], the reason for this different behavior is the different deformation of the Si–B–Si and Si–N–Si angles as a function of the strain. For strain along the e_{zz} and e_{ac} directions, these deformations are more significantly normal to the strain direction and offer the most

important contributions to the Poisson's ratio. For strain along the e_{ac} direction, these two contributions show a decrease and appear to have an almost linear dependence on strain. As a result, the Poisson's ratio also decreases and shows a similar linear dependence on strain. On the other hand, for strain along the e_{zz} direction, the contribution coming from the Si–B–Si angle deformation initially decreases (up to approximately 0.12 strain) and then shows an increase, while the contribution coming from the Si–N–Si angle deformation increases, although not linearly as a function of strain. It is thus fair to conclude that the competition between these behaviors is responsible for the behavior of the Poison's ratio as a function of strain in this case. It becomes evident that the different behavior can be attributed to the anisotropic behavior of the material due to the different bond strengths and the angles, unlike in graphene where the counterparts of the the Si–N–Si and Si–B–Si angles are the same.

E. Mechanical properties of Si$_2$BN under uniform biaxial strain. Comparison with graphene

Following the same analysis as in the previous subsection, we present in Figs. 8(a)–8(c) the strain energy per atom, ΔU, the stresses, $\sigma_{zz} = \sigma_{xx}$ and $\sigma_{ac} = \sigma_{yy}$ (stress-strain curves), and the biaxial moduli, $M_x = \sigma_{xx}/\varepsilon$ and $M_y = \sigma_{yy}/\varepsilon$, as a function of uniform biaxial strain ε for both Si$_2$BN and graphene for strains between -0.05 and their fracture limit.

Using the same methods as those described in the previous subsection, we calculate the biaxial moduli M_x and M_y. The values found from the least-squares-fitting method are, for graphene, $M_x = M_y = 1188$ GPa (or $M_x = M_y = 397$ Nt/m) and for Si$_2$BN, $M_x = 502$ GPa and $M_y = 558$ GPa (or $M_x = 168$ Nt/m and $M_y = 186$ Nt/m), which are of the order of 2/5 of the M value for graphene. Details of the fits can be found in the SM [38].

As expected, those results are consistent with the results obtained from the uniaxial strain study. According to the elasticity theory, the M_x and M_y moduli could be obtained from the Young's moduli E_x and E_y, and the Poisson's ratios ν_{xy} and ν_{yx} values, for strain along the x (or zigzag) and y (or arm chair) directions, respectively. With the notation ν_{ab}, we denote the Poisson's ratio for strain along a direction, with respect to the perpendicular in-plane direction b, i.e., $\nu_{ab} = -\varepsilon_b/\varepsilon_a$, where ε_a is the strain along the strain direction a and ε_b is the induced strain in the perpendicular in-plane direction b. The formulas derived from the elasticity theory are $M_x = E_x(1 + \nu_{yx})/(1 - \nu_{yx}\nu_{xy})$ and $M_y = E_y(1 + \nu_{xy})/(1 - \nu_{yx}\nu_{xy})$, which for the case of the isotropic graphene become $M_x = M_y = E/(1 - \nu)$. Although the derivation of those relations is rather trivial, we present it in the SM [38] for completeness. Using those formulas, the values of M_x and M_y derived for graphene are $M_x = M_y = 1190$ GPa, and for Si$_2$BN, $M_x = 480$ GPa and $M_y = 565$ GPa, differing by $\approx 4\%$ and $\approx 1\%$ for M_x and M_y of Si$_2$BN, respectively, and $\approx 0.2\%$ for graphene.

IV. CONCLUSION

In the present paper, we have studied the response of Si$_2$BN material [23], an entirely planar and kinetically stable (at least up to 1000 K) structure, to tensile uniaxial and
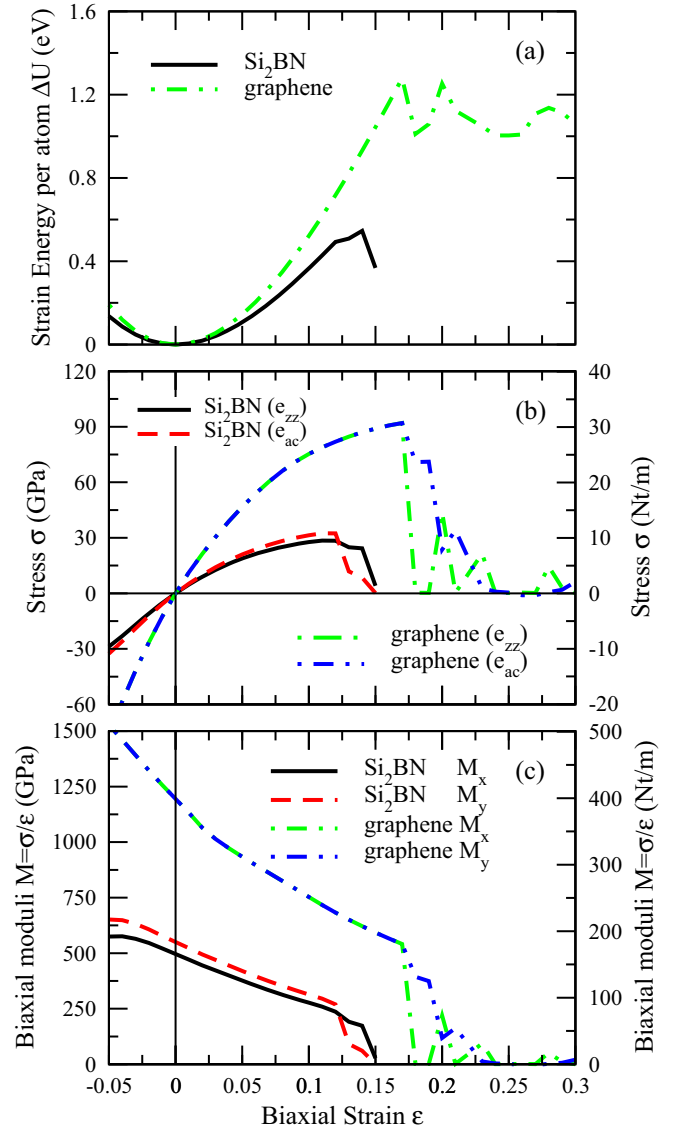

FIG. 8. Mechanical response of Si$_2$BN under uniform biaxial strain and comparison with graphene. (a) Strain energy per atom $\Delta U = (U - U_0)/N$, (b) stress-strain plot, (c) biaxial moduli $M_x = \sigma_{ac}/\varepsilon$ and $M_y = \sigma_{zz}/\varepsilon$, where σ_{ac} is the stress along the e_{ac} direction and σ_{zz} the stress along e_{zz} direction.

uniform biaxial strain up to fracture. In particular, we studied its structural deformations and its mechanical properties as a function of strain. For our paper, on the response of the structure to uniaxial strain, we selected two high-symmetry strain directions, namely the e_{zz} and e_{ac} directions, which are normal and parallel to the Si–Si bonds of the Si$_2$BN structure, respectively, and used *ab initio* DFT methods at the GGA/PBE level, as implemented in the SIESTA suite [32]. For our paper, on the response of the structure to uniform biaxial strain, the structure is strained simultaneously along both directions. For comparison, we repeated the calculations for graphene using the same method.

According to our findings, Si$_2$BN has anisotropic mechanical properties, exhibiting high Young's moduli, biaxial elastic modulus, and speed of sound values which are of the

order of 1/3, 2/5, and 3/5, respectively, of the corresponding values for graphene. The Poisson's ratio values for Si_2BN are higher by approximately 2/3 of that of graphene. Under the application of high uniaxial strain values along the e_{zz} direction, the Si–B bonds undergo bond breaking and the Si_2BN dissociates into $(Si_2BN)_2$ flake units as shown in Fig. 2, while high uniaxial strain along the e_{ac} direction causes the Si–Si bond breaking, resulting in the dissociation of the Si_2BN structure into the Si_2BN strips as shown in the same figure. For $\varepsilon > 0.27$, either for strain along the e_{zz} or the e_{ac} directions, the Si_2BN structure is deformed into the irregularly shaped structures as shown in Fig. 2 for $\varepsilon = 0.3$ and it loses its planarity. For biaxial strain, graphene breaks initially at $\varepsilon = 0.18$ into a snakelike chain, [as shown in Fig. 5(a)], but further increase of strain dissociates the structure into flakes [as shown in Fig. 5(b)]. On the other hand, Si_2BN dissociates

initially at $\varepsilon = 0.13$ into Si_2BN ribbons through the breaking of the Si–Si bonds in similar fashion to the fracture process into ribbons seen for uniaxial strain along the arm-chair direction. Further increase in the strain transforms the structure into amorphous nonplanar cluster structures, as shown in Fig. 5(f). Overall, the fracture and mechanical properties of Si_2BN are highly affected by the contrasting Si–Si and B–N bonds which are the weakest and strongest, respectively. It is worth noting that the B–N bonds do not change by more than 6% under all the studied strain conditions.

ACKNOWLEDGMENT

[1] S. Z. Butler, S. M. Hollen, L. Cao, Y. Cui, J. A. Gupta, H. R. Gutiérrez, T. F. Heinz, S. S. Hong, J. Huang, A. F. Ismach *et al.*, ACS Nano **7**, 2898 (2013).

[2] Z. G. Fthenakis and N. N. Lathiotakis, Phys. Chem. Chem. Phys. **17**, 16418 (2015).

[3] S. Trivedi, A. Srivastava, and R. Kurchania, J. Comput. Theor. Nanosci. **11**, 781 (2014).

[4] F. Schwierz, J. Pezoldt, and R. Granzner, Nanoscale **7**, 8261 (2015).

[5] H. Liu, A. T. Neal, Z. Zhu, Z. Luo, X. Xu, D. Tománek, and P. D. Ye, ACS Nano **8**, 4033 (2014).

[6] S. Zhang, J. Zhou, Q. Wang, X. Chen, Y. Kawazoe, and P. Jena, Proc. Nat. Acad. Sci. **112**, 2372 (2015).

[7] H. Şahin, S. Cahangirov, M. Topsakal, E. Bekaroglu, E. Akturk, R. T. Senger, and S. Ciraci, Phys. Rev. B **80**, 155453 (2009).

[8] Y. Ding and Y. Wang, J. Phys. Chem. C **117**, 18266 (2013).

[9] A. Hansson, F. de Brito Mota, and R. Rivelino, Phys. Rev. B **86**, 195416 (2012).

[10] M. M.S., A. K.M., and M. Valsakumar, Mech. Mater. **120**, 43 (2018).

[11] J. Dai, Y. Zhao, X. Wu, J. Yang, and X. C. Zeng, J. Phys. Chem. Lett. **4**, 561 (2013).

[12] X. Tan, C. R. Cabrera, and Z. Chen, J. Phys. Chem. C **118**, 25836 (2014).

[13] B. Feng, B. Fu, S. Kasamatsu, S. Ito, P. Cheng, C.-C. Liu, Y. Feng, S. Wu, S. K. Mahatha, P. Sheverdyaeva *et al.*, Nat. Commun. **8**, 1007 (2017).

[14] J.-W. Jiang and H. S. Park, J. Phys. D: Appl. Phys. **47**, 385304 (2014).

[15] D. Akinwande, C. J. Brennan, J. S. Bunch, P. Egberts, J. R. Felts, H. Gao, R. Huang, J.-S. Kim, T. Li, Y. Li *et al.*, Extreme Mech. Lett. **13**, 42 (2017).

[16] K. N. Kudin, G. E. Scuseria, and B. I. Yakobson, Phys. Rev. B **64**, 235406 (2001).

[17] L. Jiao, M. Hu, Y. Peng, Y. Luo, C. Li, and Z. Chen, J. Solid State Chem. **244**, 120 (2016).

[18] A. K. Geim and K. S. Novoselov, Nat. Mater. **6**, 183 (2007).

[19] K. S. Novoselov, D. Jiang, F. Schedin, T. J. Booth, V. V. Khotkevich, S. V. Morozov, and A. K. Geim, Proc. Nat. Acad. Sci. **102**, 10451 (2005).

[20] H. Nakano, T. Mitsuoka, M. Harada, K. Horibuchi, H. Nozaki, N. Takahashi, T. Nonaka, Y. Seno, and H. Nakamura, Angew. Chem. Int. Ed. **45**, 6303 (2006).

[21] Q. H. Wang, K. Kalantar-Zadeh, A. Kis, J. N. Coleman, and M. S. Strano, Nat. Nanotech. **7**, 699 (2012).

[22] Y. Lin and J. W. Connell, Nanoscale **4**, 6908 (2012).

[23] A. N. Andriotis, E. Richter, and M. Menon, Phys. Rev. B **93**, 081413(R) (2016).

[24] D. Singh, S. K. Gupta, Y. Sonvane, and R. Ahuja, Int. J. Hydrogen Energy **42**, 22942 (2017).

[25] S.-J. Yuan, H. Zhang, and X.-L. Cheng, Plasmonics **13**, 947 (2017).

[26] V. Shukla, R. B. Araujo, N. K. Jena, and R. Ahuja, Nano Energy **41**, 251 (2017).

[27] K.-X. Chen, S.-S. Lyu, Z.-Y. Luo, Y.-X. Fu, Y. Heng, and D.-C. Mo, Phys. Chem. Chem. Phys. **19**, 7481 (2017).

[28] A. Freitas, L. Machado, R. Tromer, C. Bezerra, and S. Azevedo, Superlattices Microstruct. **110**, 281 (2017).

[29] Q. Xie, J. Yuan, N. Yu, L. Wang, and J. Wang, Comput. Mater. Sci. **135**, 160 (2017).

[30] E. D. Sandoval, S. Hajinazar, and A. N. Kolmogorov, Phys. Rev. B **94**, 094105 (2016).

[31] Z. G. Fthenakis and N. N. Lathiotakis, J. Phys.: Condens. Matter **29**, 175401 (2017).

[32] J. M. Soler, E. Artacho, J. D. Gale, A. García, J. Junquera, P. Ordejón, and D. Sánchez-Portal, J. Phys.: Condens. Matter **14**, 2745 (2002).

[33] J. P. Perdew, K. Burke, and M. Ernzerhof, Phys. Rev. Lett. **77**, 3865 (1996).

[34] N. Troullier and J. L. Martins, Phys. Rev. B **43**, 1993 (1991).

[35] L. Kleinman and D. M. Bylander, Phys. Rev. Lett. **48**, 1425 (1982).

[36] GGA Pseudopotential Database, June 24, 2012, https://departments.icmab.es/leem/siesta/Databases/Pseudopotentials/periodictable-gga-abinit.html

[37] H. J. Monkhorst and J. D. Pack, Phys. Rev. B **13**, 5188 (1976).

[38] See Supplemental Material at http://link.aps.org/supplemental/10.1103/PhysRevB.99.205302 for details on the mechanical

stability analysis, least-squares fitting method to fit the stress, the Young's modulus, and the Poisson's ratio.

[39] R. Faccio, P. A. Denis, H. Pardo, C. Goyenola, and Á. W. Mombrú, J. Phys.: Condens. Matter **21**, 285304 (2009).

[40] C. Lee, X. Wei, J. W. Kysar, and J. Hone, Science **321**, 385 (2008).

[41] R. Qin, W. Zhu, Y. Zhang, and X. Deng, Nano. Res. Lett. **9**, 1 (2014).

[42] R. Qin, C.-H. Wang, W. Zhu, and Y. Zhang, AIP Adv. **2**, 022159 (2012).

[43] Y. Jing, Y. Sun, H. Niu, and J. Shen, Phys. Status Solidi B **250**, 1505 (2013).

[44] H. Zhao, Phys. Lett. A **376**, 3546 (2012).